



## Ubiquity of human-induced changes in climate variability

Keith B. Rodgers<sup>1,2</sup>, Sun-Seon Lee<sup>1,2</sup>, Nan Rosenbloom<sup>3</sup>, Axel Timmermann<sup>1,2</sup>, Gokhan Danabasoglu<sup>3</sup>, Clara Deser<sup>3</sup>, Jim Edwards<sup>3</sup>, Ji-Eun Kim<sup>1,2</sup>, Isla Simpson<sup>3</sup>, Karl Stein<sup>1,2</sup>, Malte F. Stuecker<sup>4</sup>, Ryohei Yamaguchi<sup>1,2</sup>, Tamas Bodai<sup>2</sup>, Eui-Seok Chung<sup>5</sup>, Lei Huang<sup>1,2</sup>, Who M. Kim<sup>3</sup>, Jean-François Lamarque<sup>3</sup>,  
5 Danica L. Lombardozzi<sup>3</sup>, William R. Wieder<sup>3,6</sup>, Stephen G. Yeager<sup>3</sup>

<sup>1</sup>Center for Climate Physics, Institute for Basic Science, Busan, South Korea

<sup>2</sup>Pusan National University, Busan, South Korea

<sup>3</sup>National Center for Atmospheric Research, Boulder, USA

<sup>4</sup>Department of Oceanography and International Pacific Research Center, School of Ocean and Earth Science and  
10 Technology, University of Hawai'i at Mānoa, Honolulu, HI, USA

<sup>5</sup>Korea Polar Research Institute, Incheon, South Korea

<sup>6</sup>Institute of Arctic and Alpine Research, University of Colorado, Boulder, CO, USA

*Correspondence to:* Keith B. Rodgers (krodgers@pusan.ac.kr), Axel Timmermann (axel@ibsclimate.org)

**Abstract.** While climate change mitigation targets necessarily concern maximum mean state changes, understanding impacts  
15 and developing adaptation strategies will be largely contingent on how climate variability responds to increasing anthropogenic  
perturbations. Thus far Earth system modeling efforts have primarily focused on projected mean state changes and the  
sensitivity of specific modes of climate variability, such as the El Niño-Southern Oscillation. However, our knowledge of  
forced changes in the overall spectrum of climate variability and higher order statistics is relatively limited. Here we present a  
new 100-member large ensemble of climate change projections conducted with the Community Earth System Model version  
20 2 to examine the sensitivity of internal climate fluctuations to greenhouse warming. Our unprecedented simulations reveal that  
changes in variability, considered broadly in terms of probability, distribution, amplitude, frequency, phasing, and patterns,  
are ubiquitous and span a wide range of physical and ecosystem variables across many spatial and temporal scales. Greenhouse  
warming will in particular alter variance spectra of Earth system variables that are characterized by non-Gaussian probability  
distributions, such as rainfall, primary production, or fire occurrence. Our modeling results have important implications for  
25 climate adaptation efforts, resource management, seasonal predictions, and for assessing potential stressors for terrestrial and  
marine ecosystems.



## 1 Introduction

Faced with the prospect of substantial future climate change, mitigation and adaptation strategies are increasingly paramount. While mitigation efforts are concerned chiefly with limiting mean state changes, successful adaptation will also require understanding the potentially altered variability of the climate system (Sarachik, 2010). However, the way in which climate variability will change as a result of anthropogenic radiative forcing has not been extensively explored. The spectrum of observed regional-to-global climate fluctuations is characterized by spectral variance peaks superimposed upon a broad noise background (Hasselmann, 1976; Franzke et al., 2020). These peaks are either caused by astronomical forcings or associated with spatio-temporal modes of internal climate variability (Stuecker et al., 2015), such as the El Niño-Southern Oscillation (ENSO). How modes of variability will respond to greenhouse warming has been addressed in a number of modeling studies (Timmermann et al., 1999; Cai et al., 2018), albeit with conflicting results. In contrast, the sensitivity of the spectral background to human-induced climate change is less well-known. Identifying and characterizing human-induced changes in this spectral background, using for example Climate Model Intercomparison Project (CMIP)-type coordinated modeling efforts, has proven difficult due to limited statistics.

The relatively recent advent of Large Ensemble simulations (henceforth termed Large Ensembles) conducted with Earth system models provides a new resource for addressing how climate and ecosystem statistics may evolve in response to anthropogenic forcing across a wide range of timescales (Deser et al., 2020; Schlunegger et al., 2020). Such Large Ensembles with global climate models have existed for more than 15 years (Zelle et al., 2005; Drijfhout et al., 2008; Branstator and Selten, 2009), but earlier studies expressed concern with aspects of process representation and therefore their results with regard to variability changes were inconclusive. Other studies have employed individual model simulations, small ( $\leq 10$  members) ensembles, or CMIP multi-model ensembles (Rind et al., 1989; Raisanen, 2002; Huntingford et al., 2013; Screen, 2014; Stouffer and Wetherald, 2007; Wetherald, 2009) to address whether surface temperature and precipitation variability may change under global warming. To date Large Ensemble studies of changes in variance have mainly focused on specific quantities, timescales, or regions (Deser et al., 2020; Pendergrass et al., 2017; Maher et al., 2019; Haszpra et al., 2020; Maher et al., 2021). However, to our knowledge, the full power of the Large Ensemble framework has not been applied to gauge broad-scale forced changes in climate statistics, including changes in variance, spectrum, patterns, phase, and variance, for a wide range of quantities, regions, or timescales.

To study the sensitivity of higher-order climate statistics to anthropogenic climate change, we conducted a new 100-member ensemble of climate change simulations using the Community Earth System Model version 2 (CESM2) (Danabasoglu et al., 2020), which we refer to as CESM2-LE (Methods). The initialization and forcing are described in the Methods section and in **figs. S1-S3** of the Supplementary Materials. An ensemble of this size and duration with a CMIP6-generation Earth system model at  $1^\circ$  spatial resolution is unprecedented. As such, it promises to provide an enhanced framework for documenting and understanding robust forced changes in internal variability, complementing our knowledge of mean-state changes (Simpson et al., 2020; Fasullo, 2020). The simulations were performed for the 1850-2100 period with historical (1850-2014) and SSP3-7.0 (2015-2100) forcings, and the choice of 100 members was motivated by the challenges associated with identifying trends in higher-order statistical moments (Milinski et al., 2020). To this end, substantial resources have been devoted to providing high-frequency output for the atmosphere, land, ocean, and cryosphere. Providing a clearer view of the patterns of altered climate variability should facilitate investigation of the mechanistic drivers of such changes and their implications for impacts of societal and ecosystems relevance. This study presents initial results on forced changes in internal variability across a range of quantities and timescales in CESM2-LE and will serve as the reference publication for CESM2-LE.



## 2 Methods

### 70 2.1 Model Configuration

The simulations consist of a 100-member Large Ensemble suite conducted with CESM2 with the Community Atmosphere Model version 6 (CAM6) (Danabasoglu et al., 2020), namely the CESM2-LE. The simulations which cover the period from 1850-2100 follow the historical and SSP3-7.0 forcing protocols provided by the CMIP6 (Eyring et al., 2016), although with some differences noted below for the representation of biomass burning in 50 of the 100 ensemble members. CESM2 has been demonstrated to fare well when evaluated against skill metrics with other models (Fasullo, 2020). The choice of the SSP3-7.0 scenario forcing follows CMIP6 recommendations (O'Neill et al., 2016) that emphasize the value of this « relatively high forcing level » precisely for the purpose of quantifying forced changes in natural variability. This choice should also provide a useful contribution towards an eventual CMIP6 Large Ensemble intercomparison

80 The CESM2 components use nominal 1° horizontal resolution. Specifically, CAM6 has a resolution of 1.25° in longitude and 0.9° in latitude, and 32 vertical levels with a top at 2.26 hPa, or approximately 40km. The ocean and sea-ice models are the Parallel Ocean Program version 2 (POP2) (Danabasoglu et al., 2020; Smith et al., 2010) and the CICE Version 5.1.2 (CICE5) (Bailey et al., 2020). CESM2 offers a number of improvements pertinent to our scientific interests relative to early versions of CESM1 that motivated our choice of this model. A few of the important advances with the present model configuration relative to what was available for the CESM1 Large Ensemble (Kay et al., 2015) are advances in the surface boundary layer representation for the ocean (Li et al., 2016), as well as for cloud microphysics (Gettelman et al., 2015). The ocean biogeochemistry model used with the POP2 model is the Marine Biogeochemistry Library (MARBL), which represents an updated version of what was previously known as the Biogeochemistry Elemental Cycle (Moore et al., 2001; Moore et al., 2004; Moore et al., 2013).

90 An important advance of great value to Large Ensemble investigations is achieved through new developments incorporated into the Community Land Model Version 5 (CLM5) (Danabasoglu et al., 2020; Lawrence et al., 2019; Lombardozzi et al., 2020). This model has been demonstrated to address a number of well-known limitations, including enhanced simulated cumulative CO<sub>2</sub> uptake over the historical period relative to previous versions of CLM (Bonan et al., 2019). There have also been important improvements in the implementation of the prognostic fire model and the explicit representation of agricultural management (Lombardozzi et al., 2020; Li et al., 2013; Li and Lawrence, 2017). The improvements have been extensively documented through evaluation of model simulations against the International Land Model Benchmarking (ILAMBv2.1) package (Collier et al., 2018; Danabasoglu et al., 2020; Lawrence et al., 2019). In addition to the significant improvement to net ecosystem production (NEP) highlighted in our analysis of phenology changes, improvements are found across a broad range of simulated variables in CLM5, relative to earlier versions of CLM.

### 2.2 Large Ensemble Initialization

For the CESM2-LE initialization procedure, the experimental configuration was designed to respond to broad community demand for a mix of macro- and micro-perturbations (where for micro-perturbations members differ only in a small random perturbation applied at initialization). To satisfy this demand and allow for exploration of the impact of initialization type, it was decided to initialize members from various years between 1001 and 1301 of a pre-industrial simulation conducted with CESM2 (Danabasoglu et al., 2020), as this corresponds to a time when model drift is relatively small, with the initialization procedure highlighted in **fig. S1**.

- i. Micro-initializations start from four different years: 1231, 1251, 1281, and 1301. Twenty members were runs for each start year, with ensemble spread introduced by a random perturbation to the temperature field



- 110 at initialization (commonly referred to as « pertlim »), as was used for all members of the CESM1 large ensemble (Kay et al., 2015).
- ii. Macro-initialization (one run for each initialization date) using initialization years 1001, 1011, 1021, 1031, 1041, 1051, 1061, 1071, 1081, 1091, 1101, 1111, 1121, 1131, 1141, 1151, 1161, 1171, 1181, 1191, i.e. using 20 independent restart files at 10-year intervals over 1001-1191. Note that for this case no explicit
- 115 perturbation was required from the pre-industrial control simulation. Taken together, if one includes one member from each of the micro-perturbation runs, then a total of 24 macro-perturbation runs are available. Importantly, as can be seen in **fig. S1b**, for the initialization points of years 1231, 1251, 1281, and 1301 were specifically chosen for the micro-initializations to correspond to years of maximum, decreasing, minimum, and increasing Atlantic Meridional Overturning Circulation (AMOC) transport, respectively, relative to the preindustrial control simulation. For the
- 120 analysis considered in this study, where the emphasis is on the two periods 1960-1989 and 2070-2099, we have assumed that the memory of the climate system of differences in the initial conditions from the control run (black lines in **fig. S1**) is no longer contributing to differences between ensemble members by 1950. Further quantitative exploration of the specific duration over which initial condition memory is retained is the subject of a separate ongoing study.
- 125 The macro-perturbation runs initialized in 1011, 1031, 1051, 1071, 1091, 1111, 1131, 1151, 1171, and 1191 have greatly enhanced output at high-frequency to meet the needs of broader community interests for large ensemble output. This includes 6-hourly snapshots of three-dimensional temperature, winds, and specific humidity for the Coordinated Regional Climate Downscaling Experiment (<https://cordex.org>) simulations.

### 2.3 Large Ensemble Forcing

- 130 A choice was made to use two different sets of forcing fields to represent the effects of variability in biomass burning emissions for the CESM2-LE (see **figs. S2-S3**). The biomass burning aerosol fluxes are imposed at the surface. As such, they are not prognostic, meaning that they are not generated by the model's internal prognostic fire model. The first 50 members of our Large Ensemble follow CMIP6 protocols (Van Marle et al., 2017), with biomass burning following the description in the CESM2 overview paper (Danabasoglu et al., 2020). For the second set of 50 members, which we refer to as SMBB (for
- 135 smoothed biomass burning fluxes), the CMIP6 biomass burning emissions of all relevant species for CAM6 were smoothed in time through an 11-year running mean filter. The averaging impacted variability in biomass burning fluxes over 1990-2020. The temporal smoothing of the forcing is applied to the biomass burning emissions at each grid point subsequent to being regridded to the CESM2 grid. The high 1990-2020 CMIP6 biomass burning variability (ensemble members 1-50, namely CMIP6) relative to the smoothed forcing (ensemble members 51-100, namely SMBB) has a discernable impact on large-scale
- 140 climate, as documented by the accelerated loss of September Arctic sea ice and Northern Hemispheric and tropical Pacific warming (**fig. S3a,c**).

## 3 Results

### 3.1 Mean State Changes

- During the historical period the evolution of key simulated annual-mean climate indicators in CESM2-LE (**Fig. 1; fig S4**)
- 145 agrees well with observations. The range across the ensemble members, which results from internal variability and its forced changes, spans the observed climate state much of the time, with a notable exception being Southern Ocean sea-ice (**Fig. 1e**). The results here and the general model behavior are qualitatively consistent with those of similarly-forced CMIP6-generation models (Fasullo, 2020; Kwiatkowski et al., 2020; Arora et al., 2020), although projected temperature changes (**Fig. 1c**) are in the upper range of the CMIP6 models owing to the relatively high sensitivity of CESM2 (Gettelman et al., 2019). The



150 progressive weakening of the AMOC in CESM2 over the 21<sup>st</sup> century (**Fig. 1f**) is largely consistent with other CMIP6 models  
(Weijer et al., 2020). We also find a substantial increase in land primary productivity (**Fig. 1g**), which contributes to the uptake  
of carbon in the terrestrial biosphere. Marine net primary productivity (NPP) (**Fig. 1h**) remains relatively constant throughout  
the simulation, and the overall uptake of carbon by the ocean reflects the re-emergence of anthropogenic carbon into the mixed  
layer (Toyama et al., 2017; Rodgers et al., 2020) and changes in the CO<sub>2</sub> buffering capacity of seawater (Revelle and Suess,  
155 1957). For the analysis that is presented in **Fig. 1** for sea-ice, daily-mean output fields are used for both the model and the  
data product. In representing sea-ice extent a threshold of 15% was used, whereby each grid cell is identified as being ice  
covered. For the net land fluxes of CO<sub>2</sub>, we use the variable net biome production which includes the effects of not only  
photosynthesis and respiration, but also fire and land-use change.

160 The pattern of mean state surface temperature change, shown as the difference between the periods 2070-2099 and 1960-1989  
(**Fig. 2**, central; 2m reference temperature shown in **fig. S4**), exhibits preferential warming of the eastern relative to the western  
equatorial Pacific, Arctic amplification, and a pronounced warming hole over the subpolar North Atlantic. These features are  
associated with the known mechanisms of the enhanced equatorial warming pattern (Xie et al., 2010), and more positive polar  
feedbacks (Goosse et al., 2018) including the Arctic heat capacitor (Chung et al., 2021), and the slowdown of the AMOC  
165 (Rahmstorf et al., 2015; Menary and Wood, 2018), respectively. For precipitation (**Fig. 2**, central; **fig. S4e**), changes include  
marked precipitation increases along the equatorial Pacific, within the Arctic Ocean, and decreases over the subtropical regions  
(Stocker et al., 2013).

### 3.2 Forced Changes in Amplitude, Frequency, and Phase

**Figure 2** illustrates the ensemble-aggregated Fourier amplitude spectra and probability density functions (PDFs) for five key  
170 climate and ecosystem quantities (complementary quantities are shown in **fig. S5**). For the spectral analysis in **Fig. 2**, each  
Fast Fourier Transform (FFT) spectrum is calculated for the timeseries of raw data over a given variable for the full 35-year  
interval. This includes all timescales shorter than 35 years and longer than 2 days (months) for daily (monthly) time-resolution  
data. The spectrum is calculated first at each horizontal grid point and for each ensemble member, and then averaged over the  
designated region and over the 100 ensemble members. The spectral calculations are performed to represent amplitudes of  
175 signals. The AMOC is defined as a maximum transport at 40°N. For the spectrum of internal variability of the AMOC, the  
ensemble-mean is subtracted from the raw data to remove a forced response. The surface chlorophyll concentration fields  
analyzed here represent total chlorophyll concentrations taken as a sum of diatom, diazotroph, and small phytoplankton  
chlorophyll.

180 For a wide range of Earth system variables, we find substantial changes of the projected 21<sup>st</sup> century probability distributions,  
impacting mean state, variance, and higher order statistical moments (**Fig. 2**). Human-induced alterations of climate probability  
distributions automatically translate into changes of the average return time of climate events. Averaging the spectra over 100  
ensemble members and individual grid boxes within each region creates enough data to reveal spectral characteristics that  
might otherwise be obscured. The dominant feature for most quantities examined is the spectral peak at the annual frequency,  
185 along with higher-order harmonics that result from deviations of the seasonal cycle from a pure sinusoid. Future changes of  
the annual cycle overtone spectrum can be caused by forced non-sinusoidal distortions of the annual cycle, generated e.g. by  
shifts in phenology, as discussed below. For nearly all variables under consideration, the seasonal cycle amplitude responds to  
the external forcing. Near-annual combination modes (C-modes) of ENSO and the seasonal cycle (Stuecker et al., 2015) and  
its overtones can be clearly identified in some spectra, particularly for precipitation over the equatorial Pacific. In addition to  
190 representing the C-modes as deterministic components of the system, CESM2-LE also exhibits shifts in the frequency of the  
C-modes due to future reductions in ENSO's dominant frequency (**Fig. 3a**). The C-mode peaks also strengthen in the future,



reflecting that the amplitude of precipitation and the corresponding C-mode-generating non-linearity increase at both ENSO and annual frequencies.

195 For most of the variables shown in **Fig. 2** (and **fig. S5**) there are changes in the amplitude of the spectrum across the entire range of frequencies from decadal to interannual to intra-seasonal to synoptic, revealing the ubiquity of variance changes. Importantly, frequency-independent shifts in variance can be seen in the three variables shown here, which exhibit a strong non-Gaussian skewed PDF, namely the spectra of California wildfire occurrence, surface chlorophyll concentrations over the subpolar North Atlantic (40°N-60°N, 60°W-15°W), and precipitation over the Niño3.4 region (5°S-5°N, 170°W-120°W). For  
200 these positive definite variables, which are all characterized by a highly-skewed probability distribution, forced changes in the mean state are accompanied by a stretching (squeezing) of the associated PDFs, thereby causing enhancement (or reduction) of variance and extremes. For stochastic processes, the associated variance changes manifest as timescale-independent variance changes, thereby accounting for the shown spectral background shifts. For California fire counts and Niño3.4  
205 precipitation, mean state increases are therefore also accompanied by increases in variance occurring over a wide range of timescales. For North Atlantic chlorophyll, the mean state decrease is associated with a timescale-independent decrease in variance, with expected impacts for higher trophic levels in the ocean, leading to potential disruptions to ecosystems.

For variables that are not positive-definite and less skewed, a diversity of responses is found. Forced changes in sea surface temperature (SST) variability in the Niño3.4 region are confined to interannual timescales in associated with a decrease in  
210 ENSO amplitude and a slight shift toward higher frequencies. On the other hand, for NEP over the Amazon, reflecting natural CO<sub>2</sub> exchange between the land and the atmosphere, there is an increase in variance over all timescales, accompanied by a shift in the broad interannual peak towards higher frequencies.

We next turn our attention to an expanded view of the temporal evolution of both frequency and amplitude modulations of  
215 SST and precipitation over the Niño3.4 region over the period 1960-2100. For the wavelet analysis in **Fig. 3**, we apply a Morlet wavelet normalized by  $\bar{\sigma}^{-2}$ , where  $\bar{\sigma}$  is the ensemble mean standard deviation of the respective timeseries. For analyses of patterns of changes in variance, an adjusted Welch's *t*-test (Torrence and Compo, 1998) was applied. The general approach is to first calculate the equivalent sample size  $\hat{n}$ , to account for potential serial correlations of the time series. This is then used to calculate the degrees of freedom of the Welch's *t*-test, which is an adjusted version of the Student's *t*-test that allows for the  
220 two samples to have unequal variance (i.e., heteroskedasticity). First, the decorrelation timescale  $T_e$  was calculated at each grid point, and for each period, based on the *e*-folding timescale of the autocorrelation function  $r(\tau)$ , defined as the smallest lag  $\tau$  for which  $r(\tau) < e^{-1}$ . Then the equivalent sample size  $\hat{n}$  was defined as  $\hat{n} = \frac{N}{T_e}$ , where  $N = 30$  is the total sample size in our case. The equivalent sample size was then used to calculate the degrees of freedom of the standard Welch's *t*-test. Note that this test may still be liberal if the equivalent sample sizes are small, i.e. in areas of high serial correlation.

225

Ensemble wavelet analysis of SST (**Fig. 3a**) and precipitation (**Fig. 3b**) within the Niño3.4 region has been conducted after first removing the ensemble-mean trend over the full period from each ensemble member while retaining the seasonal cycle. The wavelet analysis is conducted for each ensemble member and then averaged. We consider the normalized variance to highlight the amplification above the white noise level, and in contrast to **Fig. 2** represent variance with a linear scale to  
230 emphasize temporal modulation of the amplitude of the maxima. For SST a clear separation is seen between the maxima for interannual variability and the annual cycle (**Fig. 3a**). At interannual timescales, there are two notable features. The first is a shift in the ENSO peak period from 3.5 years to 2.5 years between the end of the 20<sup>th</sup> century and the end of the 21<sup>st</sup> century. The second feature with interannual variability is that variance does not change monotonically, but rather exhibits a maximum midway through the 21<sup>st</sup> century, similar to what has recently been reported elsewhere (Kim et al., 2014). This stands in



235 contrast to precipitation over the same region (**Fig. 3b**), for which there is a monotonic increase in variance, following a similar  
shift in the period of the peak that was found for SST. For precipitation, the amplitude of the seasonal cycle increases over  
1960-2100, consistent with the notion of variability enhancement over the tropics due to thermodynamic and dynamic  
processes (Yun et al., 2021).

240 The forced changes over 1960-2100 in the structure of the seasonal cycle for the ensemble mean of SST (**Fig. 3c**), the  
ensemble-mean of precipitation (**Fig. 3d**), the standard deviation (SD) of SST (**Fig. 3e**), and the SD of precipitation (**Fig. 3f**)  
are also considered for the Niño3.4 region using daily-mean model output. The maximum (red dots) of ensemble-mean SST  
occurs in May and the minimum (blue dots) in October in the late 20<sup>th</sup> century (**Fig. 3c**), with both showing monotonic increases  
over 1960-2100. The maximum trends to two weeks later and the minimum trends to two weeks earlier by the end of the 21<sup>st</sup>  
245 century, with this modest perturbation to the phase of the seasonal cycle being accompanied by a modulation of seasonal  
amplitude. The ensemble-mean seasonal amplitude in precipitation (**Fig. 3d**) occurs approximately one month before the  
ensemble-mean maximum in SST (**Fig. 3c**), and a second maximum in precipitation in late January becomes evident during  
the second half of the 21<sup>st</sup> century. On the other hand, the ensemble-mean minimum in precipitation occurs approximately two  
weeks after the local minimum in temperature. The increase in the amplitude of the seasonal cycle is thereby accompanied by  
250 changes in the phasing of the seasonal cycle for both SST and precipitation.

The seasonally-stratified maximum cross-ensemble SD in SST (**Fig. 3e**), associated with peak ENSO variability, exhibits a  
trend towards an earlier occurrence by approximately one month over 1960-2070. This is accompanied by a modest decrease  
in amplitude (line plot). The SD minimum for SST occurs in July for the 20<sup>th</sup> century, with a secondary minimum in the SD  
255 developing over the first half of the 21<sup>st</sup> century in May. Subsequently the SD minimum in May becomes more pronounced  
and becomes the dominant minimum in the SD of SST by the end of the 21<sup>st</sup> century. For the SD of precipitation (**Fig. 3f**),  
there is a monotonic strengthening of the seasonal maximum in late January, corresponding roughly to the time of peak ENSO  
variability, and a weakening of the seasonal minimum in October, over the interval 1960-2100. Whereas the seasonal minimum  
in the SD of precipitation (**Fig. 3f**) occurs nearly in phase with the seasonal minimum of ensemble-mean SST (**Fig. 3c**), the  
260 seasonal maximum for the SD of precipitation does not coincide with the seasonal maximum of ensemble-mean SST. Rather,  
it coincides with the secondary seasonal maximum in ensemble-mean precipitation in late January (**Fig. 3d**).

### 3.3 Changes in Variance and Co-variance Patterns

Along with modulations in the frequency domain, the spatial patterns of variance are altered in response to changing climate  
conditions. The analysis of patterns of variance and co-variance in **Fig. 4** uses cross-ensemble calculations of annual-mean  
265 standard deviations, with the cross-ensemble calculations applied for identical time records for each ensemble member. For  
the case of precipitation, averaged over December, January, February (DJF) (**Fig. 4a**), and surface temperature for DJF (**Fig.**  
**4b**), the standard deviations calculated separately over all years spanning 1960-1989 and 2070-2099 were first calculated, and  
then averaged over the two respective periods. The intention with the calculation of both standard deviations and correlations  
is to harness the full power of the Large Ensemble, and is analogous to the empirical orthogonal function (EOF) EOF-E  
270 snapshot method previously applied with empirical orthogonal functions (EOFs) (Maher et al., 2018).

We begin by considering interannual variance changes in boreal winter (December-January-February, DJF) by evaluating  
relative changes in the cross-ensemble SD of surface temperature and precipitation for the same periods as with the spectra in  
**Fig. 2** (1960-1989 and 2070-2099). The background cross-ensemble SD averaged over 1960-1989 is shown in shading (**Fig.**  
275 **4a,b**). Surface temperature (**Fig. 4a**) reveals modest decreases in variability across the equatorial Pacific and Indian Oceans,  
consistent with **Fig. 2**. Variability decreases over much of the higher latitudes of the Northern Hemisphere, with exceptions





over the Arctic and the North Atlantic, and with exceptions in the Southern Hemisphere found over Southern Africa and parts of Antarctica (**Fig. 4a**). For precipitation (**Fig. 4b**) a relative increase in SD is seen over most regions with particularly pronounced enhancements occurring in the eastern equatorial Pacific, the Indo-Pacific warm pool including the South Pacific  
280 Convergence Zone, the western Arabian Sea, the poles, and most land areas. The equatorial Pacific changes represent an eastward broadening in the centers of convection in response to the enhanced equatorial Pacific warming and the reduction of the overall zonal SST gradient (**Fig. 2, center**). In contrast, there is a decrease in the northern equatorial Atlantic Ocean as well as in some trade wind regions of the eastern Pacific.

285 Another important question to address is whether greenhouse warming can also impact the co-variability of different climate components and the global teleconnections of major modes of climate variability. This is illustrated here by examining the projected changes in the local correlation coefficients between the Niño3.4 SST index and surface temperature from 1960-1989 and 2070-2099 (**Fig. 4c**), with the background correlation coefficients shown in shading and their respective future changes shown in circles. Our analysis reveals a systematic strengthening of ENSO's remote temperature correlation over the  
290 Amazon basin and in the equatorial Atlantic, the Philippines and Japan in the western Pacific, throughout Africa, in Northern India and across eastern Canada and the Southern U.S. Co-variance decreases over western Canada and Alaska, and zonally across the equatorial Indian Ocean.

The future changes in the correlation between the Niño3.4 index and precipitation (**Fig. 4d**) indicate a pattern of enhanced co-  
295 variance over the western Pacific region surrounding the Philippines, much of Africa and South America, and western China, as documented by the background correlation coefficients and their future changes having the same sign. In other words, in these regions we see stronger ENSO teleconnections under future global warming, which in turn could translate to increased predictability of climate in the regions on seasonal to interannual timescales, but also stronger impacts. In contrast, decreased precipitation co-variance with ENSO is found for North America over the Pacific Northwest as well as much of the Southern  
300 U.S. and Mexico, as well as over Columbia/Venezuela, Bangladesh/Myanmar, parts of eastern Australia, and parts of eastern Siberia. Taken together, the global pattern of ENSO/precipitation co-variance changes (**Fig. 4d**) is due to a combination of simulated weakening of ENSO SST variability (**Fig. 4a**) and eastward expansion of the region of maximum convective activity in the equatorial Pacific (**Fig. 4b**) (analysis for the June-July August (JJA) season is shown in **fig. S6**), and likely other projected changes of the background atmospheric circulation.

### 305 3.4 Forced Changes in Phenology of Net Ecosystem Production

Finally, we illustrate how anthropogenic forcing impacts the phase of the seasonal cycle by focusing on the phenology of NEP in the Northern Hemisphere mid-to-high latitudes (over 50°N-80°N). This is motivated by ecological concerns that a shift to an earlier spring bloom, in particular over the land regions adjacent to the Arctic, can drive a phenological mismatch in ecological interactions between plants and animals (Renner and Zohner, 2018). For the seasonality/phenology analysis in the  
310 upper panel of **Fig. 5**, and area-integral of daily-mean net ecosystem production (NEP), representing the difference between gross primary productivity and ecosystem respiration, is performed over the domain 50°N-80°N for each ensemble member separately. A total of 90 ensemble members are used, as daily-mean CLM5 output was not saved for the first 10 members, namely for 1001.001, 1021.002, 11041.003, 1061.004, 1081.005, 1101.006, 1121.007, 1141.008, 1161.009, and 1181.010.

315 Ensemble-mean NEP is integrated over the region in 5-year intervals (colors in **Fig. 5**, upper panel). We find an evolving amplitude of the seasonal cycle and of the growing season length (the interval during which NEP is positive, indicating net land uptake of carbon). This representation of forced changes in the non-sinusoidal seasonal cycle reveals that the growing season length is projected to increase by approximately three weeks, with the onset shifting two weeks earlier and termination





shifting one week later. It also reveals a more than doubling of the amplitude of the seasonal cycle as a forced response. This  
320 represents an increase in the “breathing” of the terrestrial high-latitude biosphere. Information from individual ensemble  
members in 20-year intervals regarding the timing of (i) first zero crossing, (ii) maximum NEP, (iii) second zero crossing, and  
(iv) maximum negative NEP (**Fig. 5**, lower panel) reveals that interannual variability is in general smaller than the forced trend  
evident in the ensemble mean in spring. This analysis indicates that for NEP aggregated over this region the phenological shift  
as a decadal trend becomes emergent relative to estimates of the natural variability already within the first decades of the 21<sup>st</sup>  
325 century, a trend that is broadly consistent with observations (Zhu et al., 2016; Myers-Smith et al., 2020). Internal variability  
in the date of the onset of the growing season decreases by 35% over the course of the simulations and decreases by 18% for  
the date of the end of the growing season. The forced changes in growing season length are mostly attributable to changes in  
the mean temperature (Lawrence et al., 2019; Lombardozzi et al., 2020). In contrast, the internal variability in the amplitude  
of the seasonal maximum increases by 63% over the simulations, and the absolute amplitude of the seasonal minimum  
330 increases by 22% over the course of the simulations.

#### 4 Discussion

This study introduced a new, publicly available Large Ensemble of climate change simulations conducted with the global fully  
coupled CESM2 model. This Large Ensemble (CESM2-LE) is unprecedented in terms of its combination of size (100  
members), duration (1850-2100), and spatial resolution in the atmosphere and ocean (nominally 1° horizontally). As such, it  
335 affords a unique opportunity to study not only forced changes in the mean state, but also forced changes in internal variability,  
including higher-order statistical moments. Here we showcase aspects of the remarkable diversity of forced responses in  
amplitude, frequency, patterns, co-variance, and seasonal characteristics of internal variability in CESM2-LE across a broad  
suite of key physical and ecosystem quantities, spanning the atmosphere, land, cryosphere, and ocean. Importantly, and  
contrary to conventional wisdom, the changes are not solely centered on the frequency of specific climate modes such as  
340 ENSO and the Madden Julian Oscillation, but are instead broadly distributed over nearly all timescales (**Fig. 2**), in particular  
for non-Gaussian distributed variables. The mechanistic underpinnings of the changes in variability go beyond amplification  
or damping of major climate modes, and possibly include state-dependence of linear stabilities, non-linearities, rectification,  
and changes in damping timescales and noise characteristics, many of which will be investigated in forthcoming studies  
analyzing the breadth of the CESM2-LE output fields.

345 If the ubiquitous changes in variance across temporal and spatial scales described here are realized in the real world, they will  
have a number of important implications for informing adaptation strategies and assessing potential impacts. This holds for  
water resource management and agriculture, fisheries, and occurrence of wildfires. Forced changes in phenology and phasing  
of the seasonal cycle for ecosystem productivity pose risks of mismatches with trophic level interactions and energy transfers.  
350 The ubiquity of such changes in variability also points to the importance of moving beyond the assumption of stationary  
variability in detection and attribution studies of climate change (Hegerl et al., 2007), and underscores the necessity of  
recalibrating climate-economy models (Diaz and Moore, 2017) to account for an entirely different probability distribution for  
variability (**Fig. 2**, **fig. S5**) than what is currently used when projecting future climate change scenarios. The non-stationary  
nature of climate noise under anthropogenic forcing (**Fig. 2**) and the evolving teleconnections patterns (**Fig. 4**) also have  
355 implications for seasonal to multi-year climate predictability.

Although our analysis of the CESM2-LE has revealed a broad range of forced changes in variance across physical scales and  
Earth system variables, it nevertheless should be emphasized that model-uncertainty has not been considered here. There is  
already evidence for the narrower case of interannual variability in surface temperature and precipitation that model uncertainty



360 in forced changes exhibits pronounced differences between models (Maher et al., 2021) (their Supplementary Figures 7 and 8). Thus it is our hope that our work will motivate further investigations of forced change in Earth system variance across a broad range of timescales under existing archives of large ensemble simulations (Deser et al., 2020; Schlunegger et al., 2020).

Taken together, our analysis reveals an Earth system which is far more sensitive in its statistical characteristics to anthropogenic forcing than previously recognized. Although only a small fraction of such forced changes could be documented  
365 in this study, we expect that the diagnostic ensemble analysis tools applied here, along with the open access to our datasets, will inspire further investigations into the non-stationarity of Earth system processes in the presence of anthropogenic forcing.



### 370 **Code Availability**

Analysis code is available from the authors by request. The python wavelet software used for Fig. 3 was provided by Evgeniya Predybaylo (Torrence and Compo, 1998) and is available at <http://atoc.colorado.edu/research/wavelets/>.

### **Data Availability**

375 The CESM2-LE model output is available through:

<https://www.cesm.ucar.edu/projects/community-projects/LENS2/data-sets.html>

### **Author Contributions**

The CESM2-LE project was initiated by K.B.R., A.T., G.D. and C.D. The scientific framing of this manuscript was developed  
380 by K.B.R., A.T., J.-E. K., R.Y. K.S., S.-S. L. and M.F.S. Analyses and scientific post-processing were performed by R.Y., J.-  
E.K., K.S., L.H., T.B., and W. K. The CESM2-LE model runs were set up, performed, and extracted through a joint effort by  
the team of S.-S.L., N.R., and J.E. The initialization procedure for the model was developed through the joint efforts of C.D.,  
G.D., I.S., W.K., S.G.Y., and N.R. All authors discussed the results and contributed to the writing of the manuscript.

### 385 **Competing Interests**

The authors declare that they have no conflict of interest.

### **Acknowledgements**

The CESM2 Large Ensemble (CESM2-LE) simulations presented here for the first time have been conducted through a  
390 partnership between the IBS Center for Climate Physics (ICCP) in South Korea and the Community Earth System Model  
(CESM) group at the National Center for Atmospheric Research (NCAR) in the US, representing a broad collaborative effort  
between scientists from both centers.

The authors would like to thank Woncheol Roh at the ICCP and John Fasullo, Keith Lindsay, Adam S. Phillips, and Gary  
Strand at NCAR for their input and support. We would also like to thank all of the other scientists, software engineers, and  
395 administrators at both NCAR and the ICCP that contributed to this project. The framework for the macro- and micro-  
perturbation initialization strategy employed here also benefited from the US CLIVAR Workshop on Large Ensembles held  
July 2019 in Boulder CO, USA, with the support of Mike Patterson, Jennie Zhu, and Jeff Becker at US CLIVAR.

The CESM project is supported primarily by the US National Science Foundation (NSF). This material is based upon work  
supported by the NCAR, which is a major facility sponsored by the US NSF under Cooperative Agreement 1852977. The  
400 CESM2 pre-industrial control run was performed on the Cheyenne supercomputer (doi:105065/D5RX99HX) operated by the  
Computational and Information Systems Laboratory (CISL) at NCAR.

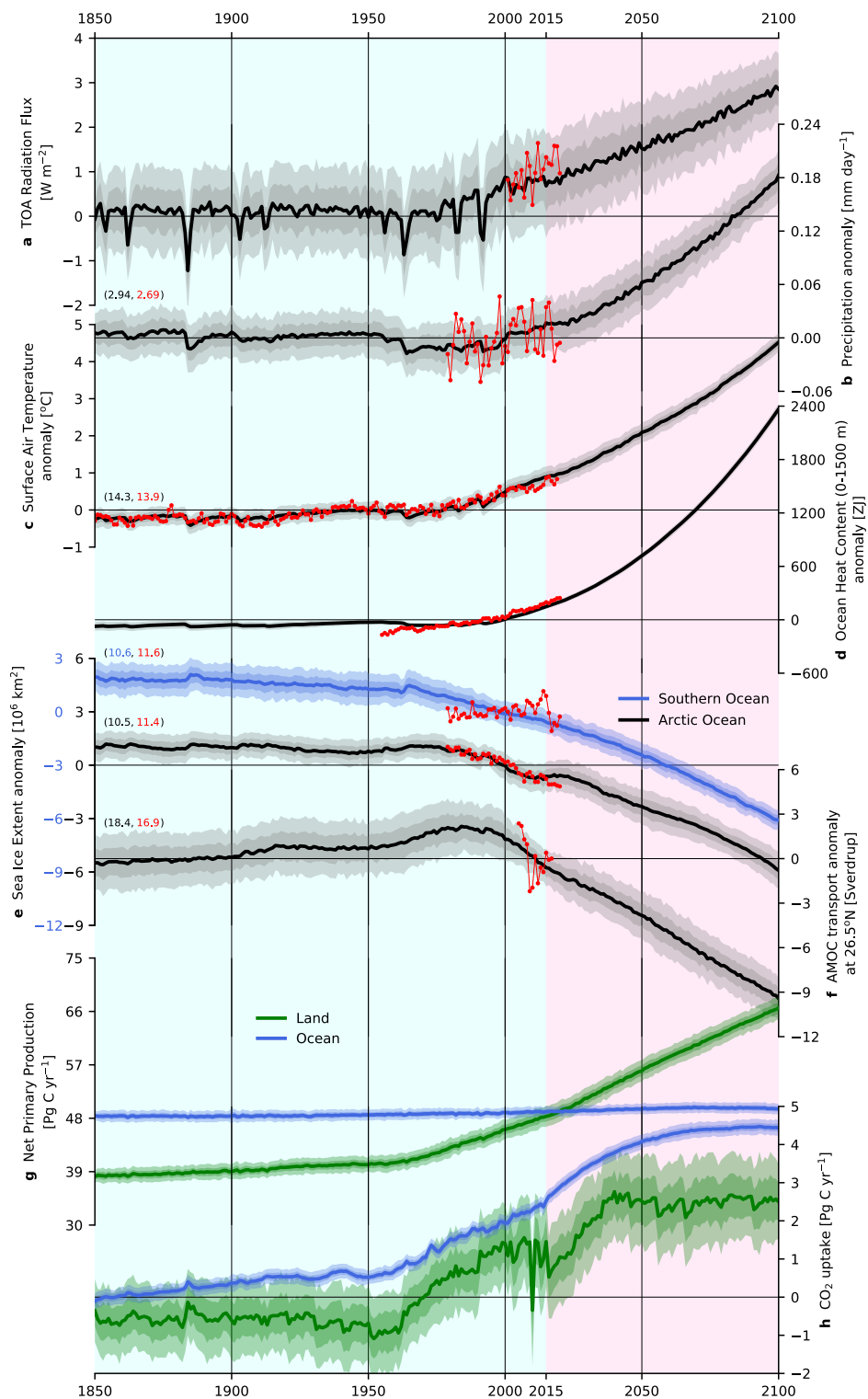
The simulations presented here were conducted on the IBS/ICCP supercomputer “Aleph”, a 1.43 petaflop high-performance  
Cray XC50-LE Skylake computing system with 18,20 processor cores, with 9.59 petabytes of disc storage, and 43 petabytes  
of tape archive storage. The CESM2-LE project duration was 15 months, and generated 5.3 petabytes of data and used  
405 approximately 200 million CPU hours of computing time.

### **Funding**

The work of K.B.R., S.-S.L, A.T., R.Y., J.-E.K., K.S., and L.H. was supported by the Institute for Basic Sciences (IBS),  
Republic of Korea, under IBS-R028-D1. T.B. was supported by the Institute for Basic Sciences (IBS), Republic of Korea,  
410 under IBS-R028-Y1. M.F.S. was supported by NOAA’s Climate Program Office’s Modeling Analysis, Predictions, and  
Projections (MAPP) program, grant NA200AR4310445 and participates in the MAPP Marine Ecosystem Task Force. This  
is IPRC publication X and SOEST contribution Y. W.R.W. and D.L.L. were supported by the National Institute of Food and  
Agriculture, US Department of Agriculture (2015-67003-23485). W.R.W. was also supported by NASA Interdisciplinary

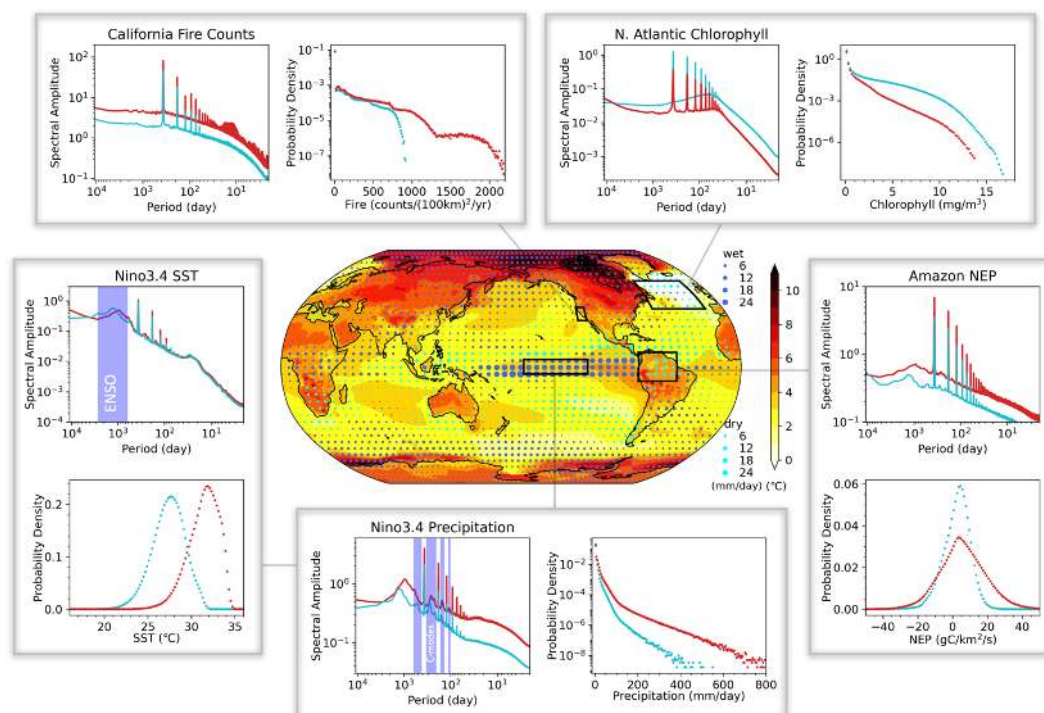


Science Program award NNX17AK19G. The work of N.R. was supported by the Regional and Global Model Analysis  
415 (RGMA) component of the Earth and Environmental System Modeling Program of the U.S. Department of Energy's Office  
of Biological and Environmental Research (BER) via National Science Foundation IA 1947282.





420 **Figure 1: Annual mean evolution of global fields over 1850-2100 for 100 ensemble members.** For model fields, bold lines  
represent ensemble means, and dark and light shading represent one standard deviation (SD) and two SD variability.  
Observational data are shown in red when appropriate. Portions of the figure with light-blue background shading indicate the  
historical period (1850-2014) while portions with light-red background shading indicate the projection period (2015-2100).  
425 (a) Top of atmosphere radiative balance ( $\text{W m}^{-2}$ ) along with the CERES-EBAF product (Loeb et al., 2018), (b) anomalies of  
the global mean precipitation ( $\text{mm day}^{-1}$ ) increasing 5.4% between the 1850s and the 2090s, compared with the Global  
Precipitation Climatology Project (GPCP) (Adler et al., 2003; Adler et al., 2012), (c) anomalies of global mean surface  
temperature, increasing by  $4.4^{\circ}\text{C}$  between the 1850s and 2090s, along with HadCRUT4 (Morice et al., 2012) anomalies over  
1950-2019, (d) anomalies of ocean heat content integrated over the upper 1500m, along with an observation-based product  
430 (Ishii et al., 2017), (e) anomalies of sea ice extent for the Arctic (black) and Southern Ocean (blue), with observed sea ice  
extent over 1979-2020 (Fetterer et al., 2017), and with the vertical scales of the anomaly plots offset to facilitate comparison,  
(f) Atlantic Meridional Overturning Circulation (AMOC) transport anomalies at  $26.5^{\circ}\text{N}$ , with RAPID array observations  
(Frajka-Williams et al., 2019), (g) globally-integrated net primary productivity (NPP) over the ocean (blue; increase of 2.7%  
between the 1850s and 2090s), and over land (green), and (h) globally-integrated net  $\text{CO}_2$  fluxes over the ocean (solid blue)  
435 and integrated net  $\text{CO}_2$  flux (net biome production, or NBP, including fire and land-use change) over land (green) with all  
quantities in (g) and (h) in units of  $\text{PgC yr}^{-1}$ . For each case, where observational products are included, anomalies are calculated  
with respect to the period spanned by the observations. For anomaly fields, printed numbers represent the absolute mean of  
the ensemble mean of CESM2-LE (black or blue numbers) and the observational product (red numbers).



440

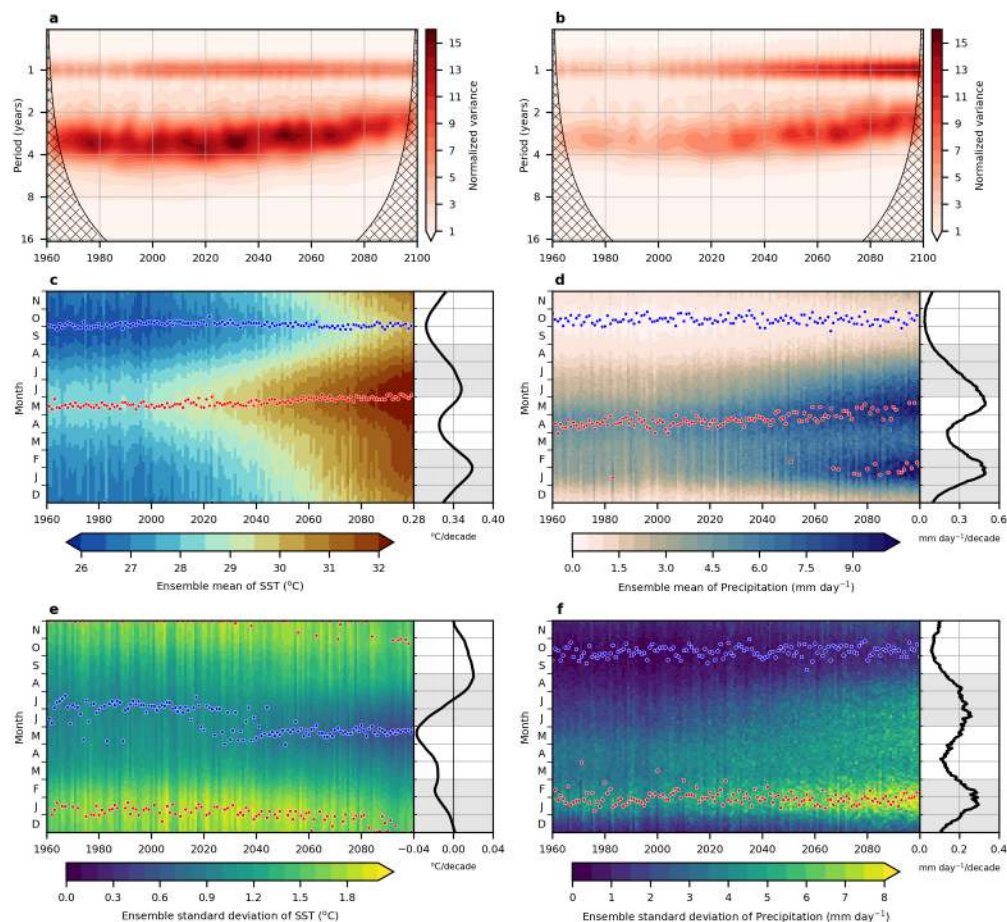
**Figure 2: Changes in the Fourier amplitude spectrum of historical (1960-1989) to future (2070-2099) climate variability in CESM2-LE.** The center map shows historical-to-future changes in surface temperature (shaded, °C) and precipitation (solid blue dots, mm day<sup>-1</sup>). Each pairing of panels shows historical (cyan) and future (red) spectra and PDFs for five different variables over four different regions. The spectra are considered over the respective periods, 1960-1989 (historical) and 2070-2099 (future), thereby including the trend, and PDFs are considered for all days over 1980-1989 and 2090-2099 to minimize the impact of the trend. From upper-left clockwise, each pair of panels shows the historical (blue) and future (red) members of fire occurrences in California (32°N-41°N, 125°W-118°W, land only), surface chlorophyll concentrations in the North Atlantic subpolar gyre (40°N-60°N, 60°W-15°W), net ecosystem production (NEP) in the Amazon (10°S-10°N, 80°W-50°W, land only), precipitation over the Niño3.4 regions (5°S-5°N, 170°W-120°W), and sea surface temperature (SST) over the Niño3.4 region. The spectra are calculated for daily timeseries at individual grid points including both forced responses and internal variability and using 30-year intervals. Subsequently the spectra are averaged over the grid points in each region. Sharp spectral peaks are associated with the annual cycle and its non-sinusoidal components, which generate high-order harmonics. Shaded areas for spectra of precipitation and temperature in the Niño3.4 region correspond to the timescales of the El Niño-Southern Oscillation (ENSO) and ENSO-annual cycle combination modes (Stuecker et al., 2013) (C-modes). Spectra are shown as amplitude, with the units being the same as the x-axes for the PDFs. PDFs of positive-definite variables (California fire counts, N. Atlantic surface chlorophyll, and Niño3.4 precipitation) are shown with logarithmic y-axes. The fields in the center panel are presented in more detail in **fig. S4**, except that there 2m reference temperature is used rather than surface temperature. A suite of complementary spectral and PDF analyses to those shown here are presented in **fig. S5**.

445

450

455





460 **Figure 3: Changes in the dominant frequencies and seasonal variance of sea surface temperature (SST, left) and**  
**precipitation (right), in the Niño3.4 region (5°S-5°N, 170°W-120°W).** (Top) The wavelet power spectra of Niño3.4 (a) SST  
 and (b) precipitation using a Morlet wavelet, normalized by  $\bar{\sigma}^{-2}$ , where  $\bar{\sigma}$  is the ensemble mean standard deviation of the  
 respective Niño3.4 time series (Torrence and Compo, 1998). The y-axis shows the equivalent Fourier period in years. The  
 hatching indicates regions where the wavelet spectrum is not trustworthy due to edge effects. Prior to calculating the wavelet  
 spectra, the time series were detrended by subtracting the ensemble-mean annual means, which were linearly interpolated to a  
 465 monthly timestep. (Middle) The ensemble-mean of Niño3.4 (c) SST and (d) precipitation indicated for each day (ordinate) and  
 year (abscissa) using daily output. The red/blue dots indicate the maximum/minimum daily values of each year. The black line  
 to the right in panels (c)-(f) indicates the linear trend over 1960-2100. (bottom) Same as for (c) and (d), but for the cross-  
 ensemble standard deviations of (e) SST and (f) precipitation.

470

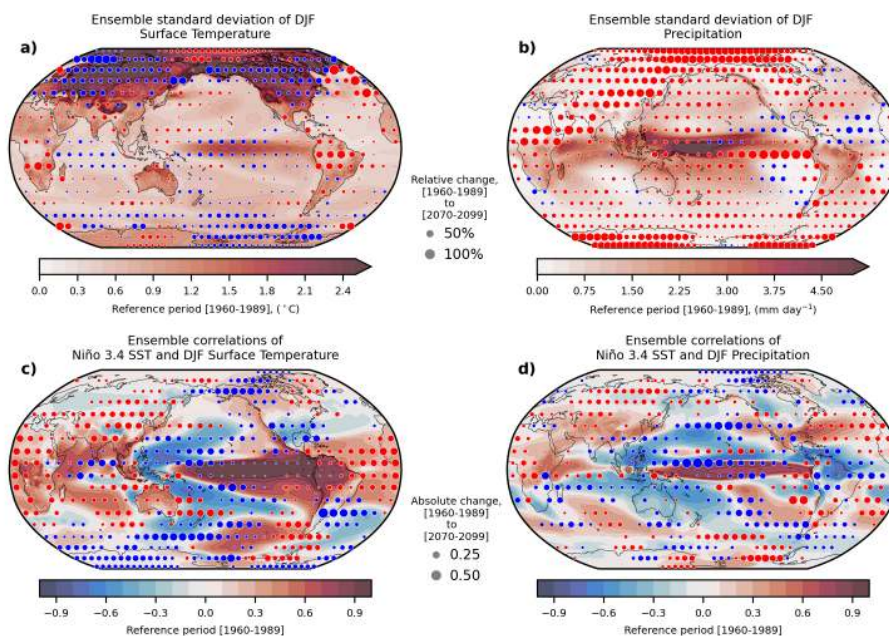


**Figure 4: Changes in the patterns of interannual variability and Niño3.4 correlation coefficients of December-January-February (DJF) surface temperature and precipitation.** (Top) Color shading shows the time-averaged absolute cross-ensemble standard deviation of the DJF seasonal mean surface temperature (a) and precipitation (b) for the period 1960-1989. Circles show the relative changes in the standard deviations between 2070-2099 and 1960-1989, where insignificant change ( $p \geq 0.05$ ) has been removed. Statistical significance of the changes (circles) was determined based on the  $p$ -values of the two-sample Welch's  $t$ -tests for the equality of temporal means of the ensemble standard deviations, with the equivalent sample sizes adjusted to account for serial correlations (Methods). (Bottom) Color shading shows ensemble-wise correlations of the Niño3.4 index with surface temperature (c) and precipitation (d) anomalies for DJF, averaged over the period 1960-1989. Circles show the absolute change in correlations between 2070-2099 and 1960-1989, where statistically insignificant changes ( $p \geq 0.05$ ) have been removed. The Niño3.4 index for ENSO is the spatial average of sea surface temperature within  $5^{\circ}\text{S}$ - $5^{\circ}\text{N}$ ,  $170^{\circ}\text{W}$ - $120^{\circ}\text{W}$ . Statistical significance of the changes (circles) was determined based on the  $p$ -values of two-sample Student's  $t$ -test of the Fisher  $z$ -transformed correlation coefficients (Timmermann et al., 2014). Note that the  $t$ -test treats the ensemble standard deviations and correlations as stationary and serially uncorrelated with either of the two periods. For all four panels, the circles represent subsampled fields at  $10^{\circ}$  intervals over the global domain. The corresponding analysis for June-July-August (JJA) is presented in **fig. S6**.

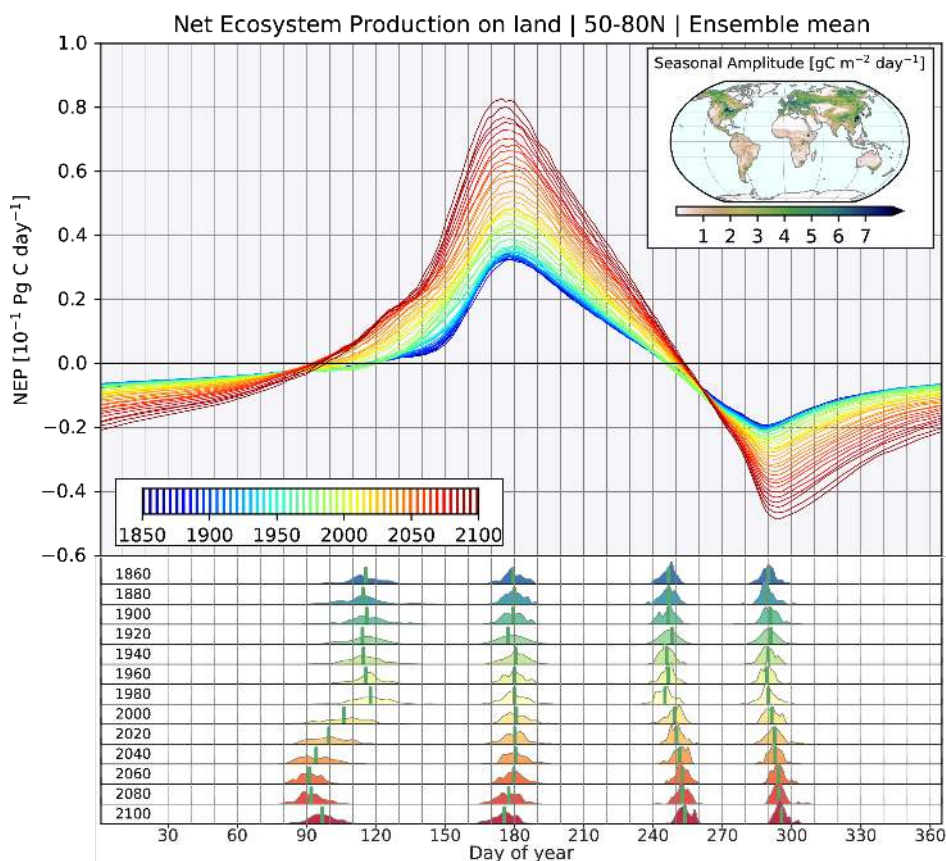


**Figure 5: Expansion of growing season length, or equivalently the carbon uptake period, over 50°N-80°N (shown here for all 90 members for which daily-mean land output was saved).** Upper panel: Evolution of ensemble mean seasonal cycle (one line for every five years, color-coded) of integrated net ecosystem productivity (NEP), with positive values indicating net terrestrial carbon uptake and negative values indicating loss of carbon from the aggregated land region. The first zero crossing marks the start of the growing seasons, and the second zero crossing marks the end of the growing seasons; Lower panel: Histograms of first occurrence of zero crossing, peak, second zero crossing, and minimum as a function of the day of year. The horizontal axis for both panels is a climatological calendar year, and aggregation is done across 90 members. The histograms represent model output sampled at 20-year intervals. The inlay map (upper right) shows the ensemble mean amplitude of the seasonal cycle of NEP averaged over 1960-1989 ( $\text{gC m}^{-2} \text{ day}^{-1}$ ).

500



## References

- Adler, R. F., Gu, G. J., and Huffman, G. J.: Estimating Climatological Bias Errors for the Global Precipitation Climatology Project (GPCP), *Journal of Applied Meteorology and Climatology*, 51, 84-99, 10.1175/jamc-d-11-052.1, 2012.
- Adler, R. F., Huffman, G. J., Chang, A., Ferraro, R., Xie, P. P., Janowiak, J., Rudolf, B., Schneider, U., Curtis, S., Bolvin, D., Gruber, A., Susskind, J., Arkin, P., and Nelkin, E.: The version-2 global precipitation climatology project (GPCP) monthly precipitation analysis (1979-present), *Journal of Hydrometeorology*, 4, 1147-1167, 10.1175/1525-7541(2003)004<1147:tvGPCP>2.0.co;2, 2003.
- Arora, V. K., Katavouta, A., Williams, R. G., Jones, C. D., Brovkin, V., Friedlingstein, P., Schwinger, J., Bopp, L., Boucher, O., Cadule, P., Chamberlain, M. A., Christian, J. R., Delire, C., Fisher, R. A., Hajima, T., Ilyina, T., Joetzjer, E., Kawamiya, M., Koven, C. D., Krasting, J. P., Law, R. M., Lawrence, D. M., Lenton, A., Lindsay, K., Pongratz, J., Raddatz, T., Seferian, R., Tachiiri, K., Tjiputra, J. F., Wiltshire, A., Wu, T. W., and Ziehn, T.: Carbon-concentration and carbon-climate feedbacks in CMIP6 models and their comparison to CMIP5 models, *Biogeosciences*, 17, 4173-4222, 10.5194/bg-17-4173-2020, 2020.
- Bailey, D. A., Holland, M. M., DuVivier, A. K., Hunke, E. C., and Turner, A. K.: Impact of a New Sea Ice Thermodynamic Formulation in the CESM2 Sea Ice Component, *Journal of Advances in Modeling Earth Systems*, 12, 15, 10.1029/2020ms002154, 2020.
- Bonan, G. B., Lombardozzi, D. L., Wieder, W. R., Oleson, K. W., Lawrence, D. M., Hoffman, F. M., and Collier, N.: Model Structure and Climate Data Uncertainty in Historical Simulations of the Terrestrial Carbon Cycle (1850-2014), *Global Biogeochemical Cycles*, 33, 1310-1326, 10.1029/2019gb006175, 2019.
- Branstator, G. and Selten, F.: "Modes of Variability" and Climate Change, *Journal of Climate*, 22, 2639-2658, 10.1175/2008jcli2517.1, 2009.
- Cai, W. J., Wang, G. J., Dewitte, B., Wu, L. X., Santoso, A., Takahashi, K., Yang, Y., Carreric, A., and McPhaden, M. J.: Increased variability of eastern Pacific El Niño under greenhouse warming, *Nature*, 564, 201-206, 10.1038/s41586-018-0776-9, 2018.
- Chung, E. S., Ha, K. J., Timmermann, A., Stuecker, M. F., Bodai, T., and Lee, S. K.: Cold-Season Arctic Amplification Driven by Arctic Ocean-Mediated Seasonal Energy Transfer, *Earths Future*, 9, 10.1029/2020ef001898, 2021.
- Collier, N., Hoffman, F. M., Lawrence, D. M., Keppel-Aleks, G., Koven, C. D., Riley, W. J., Mu, M. Q., and Randerson, J. T.: The International Land Model Benchmarking (ILAMB) System: Design, Theory, and Implementation, *Journal of Advances in Modeling Earth Systems*, 10, 2731-2754, 10.1029/2018ms001354, 2018.
- Danabasoglu, G., Lamarque, J. F., Bacmeister, J., Bailey, D. A., DuVivier, A. K., Edwards, J., Emmons, L. K., Fasullo, J., Garcia, R., Gettelman, A., Hannay, C., Holland, M. M., Large, W. G., Lauritzen, P. H., Lawrence, D. M., Lenaerts, J. T. M., Lindsay, K., Lipscomb, W. H., Mills, M. J., Neale, R., Oleson, K. W., Otto-Bliesner, B., Phillips, A. S., Sacks, W., Tilmes, S., van Kampenhou, L., Vertenstein, M., Bertini, A., Dennis, J., Deser, C., Fischer, C., Fox-Kemper, B., Kay, J. E., Kinnison, D., Kushner, P. J., Larson, V. E., Long, M. C., Mickelson, S., Moore, J. K., Nienhouse, E., Polvani, L., Rasch, P. J., and Strand, W. G.: The Community Earth System Model Version 2 (CESM2), *Journal of Advances in Modeling Earth Systems*, 12, 35, 10.1029/2019ms001916, 2020.
- Deser, C., Lehner, F., Rodgers, K. B., Ault, T., Delworth, T. L., DiNezio, P. N., Fiore, A., Frankignoul, C., Fyfe, J. C., Horton, D. E., Kay, J. E., Knutti, R., Lovenduski, N. S., Marotzke, J., McKinnon, K. A., Minobe, S., Randerson, J., Screen, J. A., Simpson, I. R., and Ting, M.: Insights from Earth system model initial-condition large ensembles and future prospects, *Nature Climate Change*, 10, 277-286, 10.1038/s41558-020-0731-2, 2020.
- Diaz, D. and Moore, F.: Quantifying the economic risks of climate change, *Nature Climate Change*, 7, 774-782, 10.1038/nclimate3411, 2017.
- Drijfhout, S., Hazeleger, W., Selten, F., and Haarsma, R.: Future changes in internal variability of the Atlantic Meridional Overturning Circulation, *Climate Dynamics*, 30, 407-419, 10.1007/s00382-007-0297-y, 2008.
- Eyring, V., Bony, S., Meehl, G. A., Senior, C. A., Stevens, B., Stouffer, R. J., and Taylor, K. E.: Overview of the Coupled Model Intercomparison Project Phase 6 (CMIP6) experimental design and organization, *Geoscientific Model Development*, 9, 1937-1958, 10.5194/gmd-9-1937-2016, 2016.
- Fasullo, J. T.: Evaluating simulated climate patterns from the CMIP archives using satellite and reanalysis datasets using the Climate Model Assessment Tool (CMATv1), *Geoscientific Model Development*, 13, 3627-3642, 2020.
- Fetterer, F., Knowles, K., Meier, W., Savoie, M., and Windnagel, A.: Sea Ice Index, version 3. National Snow and Ice Data Center, 2017.
- Frajka-Williams, E., Anson, I. J., Baehr, J., Bryden, H. L., Chidichimo, M. P., Cunningham, S. A., Danabasoglu, G., Dong, S. F., Donohue, K. A., Elipot, S., Heimbach, P., Holliday, N. P., Hummels, R., Jackson, L. C., Karstensen, J., Lankhorst, M., Le Bras, I. A., Lozier, M. S., McDonagh, E. L., Meinen, C. S., Mercier, H., Moat, B. I., Perez, R. C., Piecuch, C. G., Rhein, M., Srokosz, M. A., Trenberth, K. E., Forget, G., Goni, G., Kieke, D., Koelling, J., Lamont, T., McCarthy, G. D., Mertens, C., Send, U., Smeed, D. A., Speich, S., van den Berg, M., Volkov, D., and Wilson, C.: Atlantic Meridional Overturning Circulation: Observed Transport and Variability, *Frontiers in Marine Science*, 6, 10.3389/fmars.2019.00260, 2019.
- Franzke, C. L. E., Barbosa, S., Blender, R., Fredriksen, H. B., Laepple, T., Lambert, F., Nilsen, T., Rypdal, K., Rypdal, M., Scotto, M. G., Vannitsem, S., Watkins, N. W., Yang, L. C., and Yuan, N. M.: The Structure of Climate Variability Across Scales, *Reviews of Geophysics*, 58, 44, 10.1029/2019rg000657, 2020.
- Gettelman, A., Morrison, H., Santos, S., Bogenschutz, P., and Caldwell, P. M.: Advanced Two-Moment Bulk Microphysics for Global Models. Part II: Global Model Solutions and Aerosol-Cloud Interactions, *Journal of Climate*, 28, 1288-1307, 10.1175/jcli-d-14-00103.1, 2015.





- Gettelman, A., Hannay, C., Bacmeister, J. T., Neale, R. B., Pendergrass, A. G., Danabasoglu, G., Lamarque, J. F., Fasullo, J. T., Bailey, D. A., Lawrence, D. M., and Mills, M. J.: High Climate Sensitivity in the Community Earth System Model Version 2 (CESM2), *Geophysical Research Letters*, 46, 8329-8337, 10.1029/2019gl083978, 2019.
- Goosse, H., Kay, J. E., Armour, K. C., Bodas-Salcedo, A., Chepfer, H., Docquier, D., Jonko, A., Kushner, P. J., Lecomte, O., Massonnet, F., Park, H. S., Pithan, F., Svensson, G., and Vancoppenolle, M.: Quantifying climate feedbacks in polar regions, *Nature Communications*, 9, 10.1038/s41467-018-04173-0, 2018.
- 570 Hasselmann, K.: Stochastic Climate Models. 1. Theory, *Tellus*, 28, 473-485, 10.1111/j.2153-3490.1976.tb00696.x, 1976.
- Haszpra, T., Herein, M., and Bodai, T.: Investigating ENSO and its teleconnections under climate change in an ensemble view - a new perspective, *Earth System Dynamics*, 11, 267-280, 10.5194/esd-11-267-2020, 2020.
- Hegerl, G. C., Zwiers, F. W., Braconnot, P., Gillett, N. P., Luo, Y. M., Marengo Orsini, J. A., Nicholls, N., Penner, J. E., and Stott, P. A.: Understanding and Attributing Climate Change, in: *Climate Change 2007: The Physical Science Basis. Contribution of Working Group I to the Fourth Assessment Report of the Intergovernmental Panel on Climate Change* [Solomon, S., D. Qin, M. Manning, Z. Chen, M. Marquis, K.B. Averyt, M. Tignor and H.L. Miller (eds.)]. Cambridge University Press, Cambridge, United Kingdom and New York, NY, USA, 2007.
- 575 Huntingford, C., Jones, P. D., Livina, V. N., Lenton, T. M., and Cox, P. M.: No increase in global temperature variability despite changing regional patterns, *Nature*, 500, 327-330, 10.1038/nature12310, 2013.
- 580 Ishii, M., Fukuda, Y., Hirahara, S., Yasui, S., Suzuki, T., and Sato, K.: Accuracy of Global Upper Ocean Heat Content Estimation Expected from Present Observational Data Sets, *Sola*, 13, 163-167, 10.2151/sola.2017-030, 2017.
- Kay, J. E., Deser, C., Phillips, A., Mai, A., Hannay, C., Strand, G., Arblaster, J. M., Bates, S. C., Danabasoglu, G., Edwards, J., Holland, M., Kushner, P., Lamarque, J. F., Lawrence, D., Lindsay, K., Middleton, A., Munoz, E., Neale, R., Oleson, K., Polvani, L., and Vertenstein, M.: The Community Earth System Model (CESM) Large Ensemble Project: A Community Resource for Studying Climate Change in the Presence of Internal Climate Variability, *Bulletin of the American Meteorological Society*, 96, 1333-1349, 10.1175/bams-d-13-00255.1, 2015.
- 585 Kim, S. T., Cai, W. J., Jin, F. F., Santoso, A., Wu, L. X., Guilyardi, E., and An, S. I.: Response of El Niño sea surface temperature variability to greenhouse warming, *Nature Climate Change*, 4, 786-790, 10.1038/nclimate2326, 2014.
- Kwiatkowski, L., Torres, O., Bopp, L., Aumont, O., Chamberlain, M., Christian, J. R., Dunne, J. P., Gehlen, M., Ilyina, T., John, J. G., Lenton, A., Li, H. M., Lovenduski, N. S., Orr, J. C., Palmieri, J., Santana-Falcon, Y., Schwinger, J., Seferian, R., Stock, C. A., Tagliabue, A., Takano, Y., Tjiputra, J., Toyama, K., Tsujino, H., Watanabe, M., Yamamoto, A., Yool, A., and Ziehn, T.: Twenty-first century ocean warming, acidification, deoxygenation, and upper-ocean nutrient and primary production decline from CMIP6 model projections, *Biogeosciences*, 17, 3439-3470, 10.5194/bg-17-3439-2020, 2020.
- 590 Lawrence, D. M., Fisher, R. A., Koven, C. D., Oleson, K. W., Swenson, S. C., Bonan, G., Collier, N., Ghimire, B., van Kampenhou, L., Kennedy, D., Kluzek, E., Lawrence, P. J., Li, F., Li, H. Y., Lombardozzi, D., Riley, W. J., Sacks, W. J., Shi, M. J., Vertenstein, M., Wieder, W. R., Xu, C. G., Ali, A. A., Badger, A. M., Bisht, G., van den Broeke, M., Brunke, M. A., Burns, S. P., Buzan, J., Clark, M., Craig, A., Dahlin, K., Drewniak, B., Fisher, J. B., Flanner, M., Fox, A. M., Gentine, P., Hoffman, F., Keppel-Aleks, G., Knox, R., Kumar, S., Lenaerts, J., Leung, L. R., Lipscomb, W. H., Lu, Y. Q., Pandey, A., Pelletier, J. D., Perket, J., Randerson, J. T., Ricciuto, D. M., Sanderson, B. M., Slater, A., Subin, Z. M., Tang, J. Y., Thomas, R. Q., Martin, M. V., and Zeng, X. B.: The Community Land Model Version 5: Description of New Features, Benchmarking, and Impact of Forcing Uncertainty, *Journal of Advances in Modeling Earth Systems*, 11, 4245-4287, 10.1029/2018ms001583, 2019.
- 600 Li, F. and Lawrence, D. M.: Role of Fire in the Global Land Water Budget during the Twentieth Century due to Changing Ecosystems, *Journal of Climate*, 30, 1893-1908, 10.1175/jcli-d-16-0460.1, 2017.
- 605 Li, F., Levis, S., and Ward, D. S.: Quantifying the role of fire in the Earth system - Part 1: Improved global fire modeling in the Community Earth System Model (CESM1), *Biogeosciences*, 10, 2293-2314, 10.5194/bg-10-2293-2013, 2013.
- Li, Q., Webb, A., Fox-Kemper, B., Craig, A., Danabasoglu, G., Large, W. G., and Vertenstein, M.: Langmuir mixing effects on global climate: WAVEWATCH III in CESM, *Ocean Modelling*, 103, 145-160, 10.1016/j.ocemod.2015.07.020, 2016.
- 610 Loeb, N. G., Wielicki, B. A., Doelling, D. R., Smith, G. L., Keyes, D. F., Kato, S., Manalo-Smith, N., and Wong, T.: Toward Optimal Closure of the Earth's Top-of-Atmosphere Radiation Budget, *Journal of Climate*, 22, 748-766, 10.1175/2008jcli2637.1, 2009.
- Loeb, N. G., Doelling, D. R., Wang, H. L., Su, W. Y., Nguyen, C., Corbett, J. G., Liang, L. S., Mitrescu, C., Rose, F. G., and Kato, S.: Clouds and the Earth's Radiant Energy System (CERES) Energy Balanced and Filled (EBAF) Top-of-Atmosphere (TOA) Edition-4.0 Data Product, *Journal of Climate*, 31, 895-918, 10.1175/jcli-d-17-0208.1, 2018.
- 615 Lombardozzi, D. L., Lu, Y. Q., Lawrence, P. J., Lawrence, D. M., Swenson, S., Oleson, K. W., Wieder, W. R., and Ainsworth, E. A.: Simulating Agriculture in the Community Land Model Version 5, *Journal of Geophysical Research-Biogeosciences*, 125, 19, 10.1029/2019jg005529, 2020.
- Maher, N., Power, S. B., and Marotzke, J.: More accurate quantification of model-to-model agreement in externally forced climatic responses over the coming century, *Nature Communications*, 12, 13, 10.1038/s41467-020-20635-w, 2021.
- 620 Maher, N., Matei, D., Milinski, S., and Marotzke, J.: ENSO Change in Climate Projections: Forced Response or Internal Variability?, *Geophysical Research Letters*, 45, 11390-11398, 10.1029/2018gl079764, 2018.
- Maher, N., Milinski, S., Suarez-Gutierrez, L., Botzet, M., Dobrynin, M., Kornbluh, L., Kroger, J., Takano, Y., Ghosh, R., Hedemann, C., Li, C., Li, H. M., Manzini, E., Notz, D., Putrasahan, D., Boysen, L., Claussen, M., Ilyina, T., Olonscheck, D., Raddatz, T., Stevens, B., and Marotzke, J.: The Max Planck Institute Grand Ensemble: Enabling the Exploration of Climate System Variability, *Journal of Advances in Modeling Earth Systems*, 11, 2050-2069, 10.1029/2019ms001639, 2019.
- 625 Menary, M. B. and Wood, R. A.: An anatomy of the projected North Atlantic warming hole in CMIP5 models, *Climate Dynamics*, 50, 3063-3080, 10.1007/s00382-017-3793-8, 2018.



- Milinski, S., Maher, N., and Olonscheck, D.: How large does a large ensemble need to be?, *Earth System Dynamics*, 11, 885-901, 10.5194/esd-11-885-2020, 2020.
- 630 Moore, J. K., Doney, S. C., and Lindsay, K.: Upper ocean ecosystem dynamics and iron cycling in a global three-dimensional model, *Global Biogeochemical Cycles*, 18, 21, 10.1029/2004gb002220, 2004.  
Moore, J. K., Doney, S. C., Kleypas, J. A., Glover, D. M., and Fung, I. Y.: An intermediate complexity marine ecosystem model for the global domain, *Deep-Sea Research Part II-Topical Studies in Oceanography*, 49, 403-462, 10.1016/s0967-0645(01)00108-4, 2001.
- 635 Moore, J. K., Lindsay, K., Doney, S. C., Long, M. C., and Misumi, K.: Marine Ecosystem Dynamics and Biogeochemical Cycling in the Community Earth System Model CESM1(BGC) : Comparison of the 1990s with the 2090s under the RCP4.5 and RCP8.5 Scenarios, *Journal of Climate*, 26, 9291-9312, 10.1175/jcli-d-12-00566.1, 2013.  
Morice, C. P., Kennedy, J. J., Rayner, N. A., and Jones, P. D.: Quantifying uncertainties in global and regional temperature change using an ensemble of observational estimates: The HadCRUT4 data set, *Journal of Geophysical Research-Atmospheres*, 117, 22, 10.1029/2011jd017187, 2012.
- 640 Myers-Smith, I. H., Kerby, J. T., Phoenix, G. K., Bjerke, J. W., Epstein, H. E., Assmann, J. J., John, C., Andreu-Hayles, L., Angers-Blondin, S., and Beck, P. S.: Complexity revealed in the greening of the Arctic, *Nature Climate Change*, 10, 106-117, 2020.  
O'Neill, B. C., Tebaldi, C., van Vuuren, D. P., Eyring, V., Friedlingstein, P., Hurtt, G., Knutti, R., Kriegler, E., Lamarque, J. F., Lowe, J., Meehl, G. A., Moss, R., Riahi, K., and Sanderson, B. M.: The Scenario Model Intercomparison Project (ScenarioMIP) for CMIP6, *Geoscientific Model Development*, 9, 3461-3482, 10.5194/gmd-9-3461-2016, 2016.  
Pendergrass, A. G., Knutti, R., Lehner, F., Deser, C., and Sanderson, B. M.: Precipitation variability increases in a warmer climate, *Scientific Reports*, 7, 9, 10.1038/s41598-017-17966-y, 2017.  
Rahmstorf, S., Box, J. E., Feulner, G., Mann, M. E., Robinson, A., Rutherford, S., and Schaffernicht, E. J.: Exceptional twentieth-century slowdown in Atlantic Ocean overturning circulation, *Nature Climate Change*, 5, 475-480, 10.1038/nclimate2554, 2015.
- 650 Raisanen, J.: CO<sub>2</sub>-induced changes in interannual temperature and precipitation variability in 19 CMIP2 experiments, *Journal of Climate*, 15, 2395-2411, 10.1175/1520-0442(2002)015<2395:ciciit>2.0.co;2, 2002.  
Renner, S. S. and Zohner, C. M.: Climate Change and Phenological Mismatch in Trophic Interactions Among Plants, Insects, and Vertebrates, *Annual Review of Ecology, Evolution, and Systematics*, Vol 49, 49, 165-182, 10.1146/annurev-ecolsys-110617-062535, 2018.  
Revelle, R. and Suess, H. E.: Carbon Dioxide Exchange Between Atmosphere and Ocean and the Question of an Increase of Atmospheric CO<sub>2</sub> During the Past Two Decades, *Tellus*, 9, 18-27, 1957.
- 660 Rind, D., Goldberg, R., and Ruedy, R.: Change in Climate Variability in the 21st-Century, *Climatic Change*, 14, 5-37, 10.1007/bf00140173, 1989.  
Rodgers, K. B., Schlunegger, S., Slater, R. D., Ishii, M., Frolicher, T. L., Toyama, K., Plancherel, Y., Aumont, O., and Fassbender, A. J.: Reemergence of Anthropogenic Carbon Into the Ocean's Mixed Layer Strongly Amplifies Transient Climate Sensitivity, *Geophysical Research Letters*, 47, 9, 10.1029/2020gl089275, 2020.  
Sarachik, E. S.: The tools of adaptation, *Second International Conference on Climate, Sustainability, and Development in Semi-Arid Regions*, Fortaleza, Brazil2010.
- 665 Schlunegger, S., Rodgers, K. B., Sarmiento, J. L., Ilyina, T., Dunne, J. P., Takano, Y., Christian, J. R., Long, M. C., Frolicher, T. L., Slater, R., and Lehner, F.: Time of Emergence and Large Ensemble Intercomparison for Ocean Biogeochemical Trends, *Global Biogeochemical Cycles*, 34, 18, 10.1029/2019gb006453, 2020.  
Screen, J. A.: Arctic amplification decreases temperature variance in northern mid- to high-latitudes, *Nature Climate Change*, 4, 577-582, 10.1038/nclimate2268, 2014.
- 670 Simpson, I. R., Bacmeister, J., Neale, R. B., Hannay, C., Gettelman, A., Garcia, R. R., Lauritzen, P. H., Marsh, D. R., Mills, M. J., Medeiros, B., and Richter, J. H.: An Evaluation of the Large-Scale Atmospheric Circulation and Its Variability in CESM2 and Other CMIP Models, *Journal of Geophysical Research-Atmospheres*, 125, 42, 10.1029/2020jd032835, 2020.  
Smith, R., Jones, P., Briegleb, B., Bryan, F., Danabasoglu, G., Dennis, J., Dukowicz, J., Eden, C., Fox-Kemper, B., Gent, P., Hecht, M., Jayne, S., Jochum, M., Large, W., Lindsay, K., Maltrud, M., Norton, N., Peacock, S., Vertenstein, M., and Yeager, S.: The Parallel Ocean Program (POP) Reference Manual, *Ocean Component of the Community Climate System Model (CCSM)*, 2010.
- 675 Stocker, T., Intergovernmental Panel on Climate Change, W. G. I., WMO, and UNEP: *Climate Change 2013: The Physical Science Basis: Working Group I Contribution to the 5th Assessment Report of the Intergovernmental Panel on Climate Change*, 2013.  
Stouffer, R. J. and Wetherald, R. T.: Changes of variability in response to increasing greenhouse gases. Part I: Temperature, *Journal of Climate*, 20, 5455-5467, 10.1175/2007jcli1384.1, 2007.  
Stuecker, M. F., Jin, F. F., and Timmermann, A.: El Niño-Southern Oscillation frequency cascade, *Proceedings of the National Academy of Sciences of the United States of America*, 112, 13490-13495, 10.1073/pnas.1508622112, 2015.
- 685 Stuecker, M. F., Timmermann, A., Jin, F. F., McGregor, S., and Ren, H. L.: A combination mode of the annual cycle and the El Niño/Southern Oscillation, *Nature Geoscience*, 6, 540-544, 10.1038/ngeo1826, 2013.  
Timmermann, A., Sachs, J., and Timm, O. E.: Assessing divergent SST behavior during the last 21 ka derived from alkenones and G. ruber-Mg/Ca in the equatorial Pacific, *Paleoceanography*, 29, 680-696, 10.1002/2013pa002598, 2014.  
Timmermann, A., Oberhuber, J., Bacher, A., Esch, M., Latif, M., and Roeckner, E.: Increased El Niño frequency in a climate model forced by future greenhouse warming, *Nature*, 398, 694-697, 1999.
- 690



- Torrence, C. and Compo, G. P.: A practical guide to wavelet analysis, *Bulletin of the American Meteorological Society*, 79, 61-78, 10.1175/1520-0477(1998)079<0061:apgtwa>2.0.co;2, 1998.
- Toyama, K., Rodgers, K. B., Blanke, B., Iudicone, D., Ishii, M., Aumont, O., and Sarmiento, J. L.: Large Reemergence of Anthropogenic Carbon into the Ocean's Surface Mixed Layer Sustained by the Ocean's Overturning Circulation, *Journal of Climate*, 30, 8615-8631, 10.1175/jcli-d-16-0725.1, 2017.
- 695 van Marle, M. J. E., Kloster, S., Magi, B. I., Marlon, J. R., Daniiau, A. L., Field, R. D., Arneeth, A., Forrest, M., Hantson, S., Kehrwald, N. M., Knorr, W., Lasslop, G., Li, F., Mangeon, S., Yue, C., Kaiser, J. W., and van der Werf, G. R.: Historic global biomass burning emissions for CMIP6 (BB4CMIP) based on merging satellite observations with proxies and fire models (1750-2015), *Geoscientific Model Development*, 10, 3329-3357, 10.5194/gmd-10-3329-2017, 2017.
- 700 Weijer, W., Cheng, W., Garuba, O. A., Hu, A., and Nadiga, B. T.: CMIP6 Models Predict Significant 21st Century Decline of the Atlantic Meridional Overturning Circulation, *Geophysical Research Letters*, 47, 10.1029/2019gl086075, 2020.
- Wetherald, R. T.: Changes of Variability in Response to Increasing Greenhouse Gases. Part II: Hydrology, *Journal of Climate*, 22, 6089-6103, 10.1175/2009jcli2834.1, 2009.
- Xie, S. P., Deser, C., Vecchi, G. A., Ma, J., Teng, H. Y., and Wittenberg, A. T.: Global Warming Pattern Formation: Sea Surface Temperature and Rainfall, *Journal of Climate*, 23, 966-986, 10.1175/2009jcli3329.1, 2010.
- 705 Yun, K. S., Lee, J. Y., Timmermann, A., Stein, K., Stuecker, J. F., Fyfe, J. C., and Chung, E. S.: Increasing ENSO-rainfall variability due to changes in future tropical temperature-rainfall relationship, *Communications Earth & Environment*, 2, 1-7, 2021.
- Zelle, H., Van Oldenborgh, G. J., Burgers, G., and Dijkstra, H.: El Niño and Greenhouse warming: Results from ensemble simulations with the NCAR CCSM, *Journal of Climate*, 18, 4669-4683, 10.1175/jcli3574.1, 2005.
- 710 Zhu, Z. C., Piao, S. L., Myneni, R. B., Huang, M. T., Zeng, Z. Z., Canadell, J. G., Ciais, P., Sitch, S., Friedlingstein, P., Arneeth, A., Cao, C. X., Cheng, L., Kato, E., Koven, C., Li, Y., Lian, X., Liu, Y. W., Liu, R. G., Mao, J. F., Pan, Y. Z., Peng, S. S., Penuelas, J., Poulter, B., Pugh, T. A. M., Stocker, B. D., Viovy, N., Wang, X. H., Wang, Y. P., Xiao, Z. Q., Yang, H., Zaehle, S., and Zeng, N.: Greening of the Earth and its drivers, *Nature Climate Change*, 6, 791-795, 10.1038/nclimate3004, 2016.
- 715